

D2C-SR: A Divergence to Convergence Approach for Real-World Image Super-Resolution

Youwei Li¹ Haibin Huang² Lanpeng Jia¹ Haoqiang Fan¹ Shuaicheng Liu^{1,3}

¹Megvii Technology

{liyouwei, jialanpeng, fhq, liushuaicheng}@megvii.com

²Kuaishou Technology

jackiehuanghaibin@gmail.com

³University of Electronic Science and Technology of China

liushuaicheng@uestc.edu.cn

Abstract

In this paper, we present D2C-SR, a novel framework for the task of real-world image super-resolution. As an ill-posed problem, the key challenge in super-resolution related tasks is there can be multiple predictions for a given low-resolution input. Most classical deep learning based approaches ignored the fundamental fact and lack explicit modeling of the underlying high-frequency distribution which leads to blurred results. Recently, some methods of GAN-based or learning super-resolution space can generate simulated textures but do not promise the accuracy of the textures which have low quantitative performance. Rethinking both, we learn the distribution of underlying high-frequency details in a discrete form and propose a two-stage pipeline: divergence stage to convergence stage. At divergence stage, we propose a tree-based structure deep network as our divergence backbone. Divergence loss is proposed to encourage the generated results from the tree-based network to diverge into possible high-frequency representations, which is our way of discretely modeling the underlying high-frequency distribution. At convergence stage, we assign spatial weights to fuse these divergent predictions to obtain the final output with more accurate details. Our approach provides a convenient end-to-end manner to inference. We conduct evaluations on several real-world benchmarks, including a new proposed D2CRealSR dataset with x8 scaling factor. Our experiments demonstrate that D2C-SR achieves better accuracy and visual improvements against state-of-the-art methods, with a significantly less parameters number.

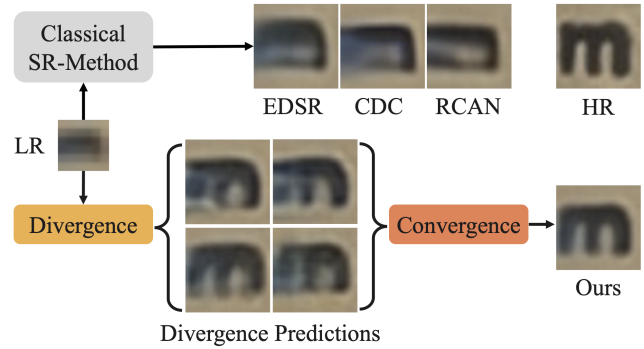


Figure 1. Classical SR methods directly use a single prediction to fit the distribution of all high-frequency details, thus obtain blurred outputs due to the ill-posed nature. Our two-stage approach explicitly learns the distribution of high-frequency details using a discrete manner, thus we can get rich and accurate texture details.

1. Introduction

Super-resolution (SR) is one of the fundamental problems in computer vision with its applications for several important image processing tasks. Despite decades of development in image SR technologies, it remains challenging to recover high-quality and accurate details from low-resolution (LR) inputs due to its ill-posed nature.

In fact, given a LR image, there exist infinitely possible high-resolution (HR) predictions by adding different high-frequency information. This is the key challenge for the design of learning-based SR methods. Recently, deep neural network (DNN) based methods [20, 13, 33, 16, 21] have achieved tremendous success and outperformed most classical methods based on sparse coding [31, 7] or local linear regression [30, 24]. However, these early deep learning methods only rely on L_1 or L_2 reconstruction loss,

which have a relatively high quantitative performance but can not reproduce rich texture details due to ill-posed nature. Later on, conditional GAN-based methods [8] are adapted into SR tasks, which provide methods for learning the distribution in a data-driven way and led to generate richer simulated textures. However, these methods still suffered from mode collapse and tend to generate implausible or inaccurate texture details. Thus, the quantitative performance of GAN-based methods are not satisfactory. After realizing the importance of modeling the underlying high-frequency distribution explicitly, some methods of learning SR space appear. SRFflow [14] introduced a normalizing flow-based method which tried to address the mode collapse problem and make a continuous Gaussian distribution to model all the high-frequency. Therefore, although SRFflow can sample to get a certain prediction, it does not promise the most accurate prediction. Furthermore, when adapting more complicated distribution, like large amount of real-world scenes, it would significantly increase the hardness of convergence during training. Some works [11, 25, 29, 17] introduced ensemble-based SR approaches that trained a same network from different initialization or different down-sampling methods and merged the outputs into the SR results. Due to the lack of explicit modeling of the SR space, these methods still lead to unsatisfactory results like over-smooth effects, which is caused by the ill-posed nature.

In this paper, we present D2C-SR, a novel divergence to convergence framework for real-world SR, by rethinking the ill-posed problem and the SR space approaches. D2C-SR follows the idea of explicitly learning the underlying distribution of high-frequency details. But unlike conditional GAN-based methods or SRFflow, our D2C-SR model the high-frequency details distribution using a discrete manner. Our key insight is that: most classical SR methods use a single output to fit all high-frequency details directly and therefore only obtains average and blurred outputs, while SRFflow uses an continuous Gaussian distribution to fit all high-frequency details, but the fit is very difficult and does not guarantee stable and accurate high-frequency details. Therefore, we adopt a trade-off approach by using a finite discrete distribution to fit the high-frequency details, thus ensuring a stable, controllable and accurate output relatively. Specifically, at divergence stage, we first propose a tree-based structure network, where end branches are designed to learn possible high-frequency details. We use the modified triplet loss to enforce the outputs from different branches are divergent, meanwhile, together with a construction loss to ensure consistency with HR. Theoretically, if there are multiple branches and fit to the full range of high-frequency possibilities, the best HR image should be the fusion of the high-frequency details exactly. Hence, at convergence stage, we assign spatial weights to combine

the divergent predictions to produce a more accurate result. To fully evaluate the efficiency and generality of D2C-SR for real-world SISR, we conduct experiments on several benchmarks, including RealSR[5], DRealSR[28] and our new benchmark, D2CRealSR, with x8 upscaling factor. Experimental results show that our D2C-SR can achieve state-of-the-art performance and visual improvements with less parameter number. To summarize, the main contributions are as follows:

- We present D2C-SR, a novel framework with divergence stage and convergence stage for real-world SR. D2C-SR explicitly model the underlying distribution of high-frequency details in a discrete manner and provide a convenient way for end-to-end inference.
- We propose the divergence loss to generated multiple results with divergent high-frequency representations.
- A new real-world SR benchmark (D2CRealSR), which has a larger scaling factor (x8) compared to existing real-world SR benchmarks.
- D2C-SR sets up new state-of-the-art performance on many popular real-world SR benchmarks, including our new proposed D2CRealSR benchmark. D2C-SR can also provide compatible performance with significantly less parameter number.

2. Related Work

2.1. DNN-based SISR

Single Image Super Resolution (SISR) is a long standing research topic due to its importance and ill-posed nature. Traditional learning-based methods adopts sparse coding [7, 22, 31] or local linear regression [24, 23, 30]. Deep learning (DL)-based methods have achieved dramatic advantages against conventional methods for SISR [27, 1]. It is first proposed by SRCNN [20] that employs a relatively shallow network and adopts the bicubic degradation for HR and LR pairs. Following which, various SISR approaches have been proposed, such as VDSR that adopts very deep network [20]; EDSR that modifies the ResNet for enhancement [13]; ESPCN that uses efficient sub-pixel CNN [19]; CDC that divides images into multiple regions [28], and VGG loss [20], GAN loss [8] that improve the perceptual visual quality [12, 18, 26]. Ensemble-based methods [11, 25, 29, 17] train a same network from different initialization or different training pair generation but it lacks explicit modeling of SR space. In this work, we propose a tree-based network structure, for the purpose of multi-mode learning.

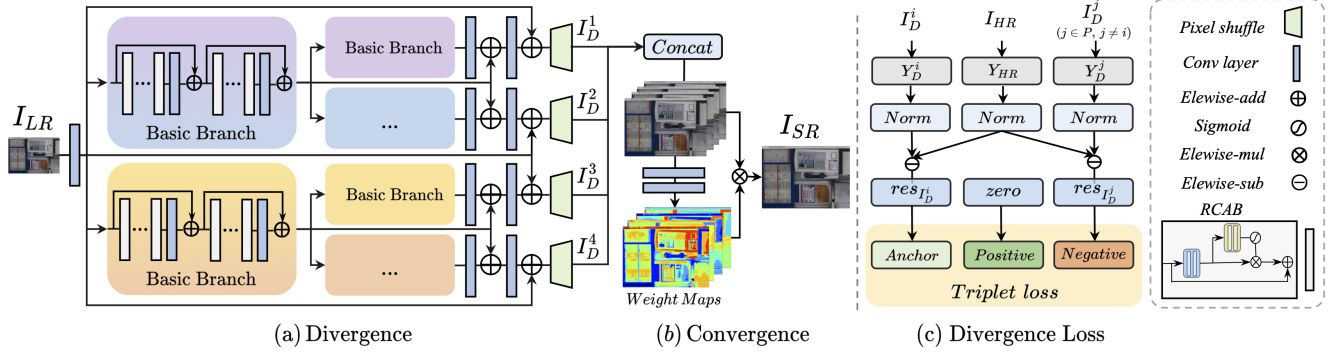


Figure 2. Our architecture consists of two stages, (a) Divergence stage and (b) Convergence stage. The divergence network with tree structure outputs multiple predictions I_D^i who has different high-frequency recovery. The goal of convergence network is to obtain more accurate result SR by weighted combining the results. (c) Divergence loss is used to train our network.

2.2. Learning Super Resolution Space

Single image super-resolution is ill-posed, where infinitely many high-resolution images can be downsampled to the same low-resolution images. Therefore learning a deterministic mapping may not be optimal. The problem can be converted to stochastic mapping, where multiple plausible high-resolution images are predicted given a single low-resolution input [2]. DeepSEE incorporates semantic maps for explorative facial super-resolution [4]. SRFflow adopts normalizing flow to learn the high-frequency distribution of facial datasets by using an continuous Gaussian distribution [14]. Unlike this, our method model the high-frequency distribution using a discrete manner. Thus the prediction of our method has better texture consistency with HR and the details are more accurate.

2.3. Real-World Super Resolution and Datasets

Bicubic downsampling datasets are widely used but the gap between the simulation and the real degradation limits the performance in the real-world application [9]. Therefore, some works explore degradation of real scenarios by collecting real-world datasets, e.g., City100 [6], RealSR [5], SR-RAW [32] and DRealSR [28]. We propose the D2CRealSR dataset with larger scaling factor (x8) compared to the above datasets. Real-world degradation loses more details compared to simulated degradation [6], and the reduction of the prior makes recovery more difficult. Our method can handle these problems better than other methods. In addition, we still conducted some experiments on bicubic datasets. More details in the supplementary material.

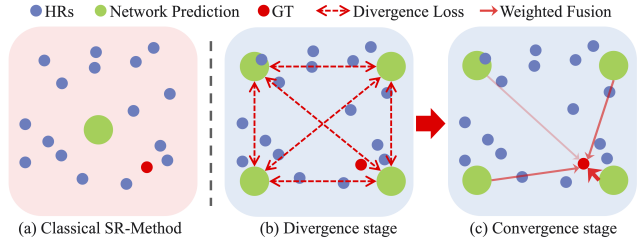


Figure 3. Difference between our method and the classical method in handling ill-posed problems. Blue dots in the box indicate multiple possible HR texture details for a settled LR region. Red dots indicate the ground-truth details. The classical method can only find the single average prediction. However, our method can produce multiple divergent predictions at divergence stage and fuse to obtain more accurate predictions at convergence stage.

3. Method

3.1. Overview

As shown in Fig. 2, D2C-SR consists of two sub-networks: a divergence network to learn the possible predictions and a convergence network to fuse the predictions to final result. In this section, we first describe divergence network in Sec. 3.2. Then, we introduce convergence network in Sec. 3.3. The network training strategy are described in Sec. 3.4. To facilitate the explanation of our approach, we also present in Figure 3.

3.2. Divergence Network

Divergence network produce multiple divergent predictions to address the ill-posed nature. We built a tree-based structure network to get the desired predictions. There are four main modules in the divergence network: shallow feature extraction, basic branch module, deep residual structure and upscale module. We define the depth of the tree network is L , and each branch has C sub-branches. Each

branch and its sub-branches are composed of a basic branch module and non-weight shared. Further, the basic branch module contains G residual groups, and each residual group contains B residual channel attention blocks, which refer to RCAN [33]. The divergence network first extracts the shallow features from the input LR image by the shallow feature extraction module, which is a simple Conv layer. Then, the input features are each fed into their own branch and sub-branches modules. The feature outputs of the end branches go through the deep residual structure, then upscaled by the upscale module. So far, the divergence network generate P divergent predictions. These predictions are expressed as $I_D = \mathcal{F}(I_{LR}; \Theta_D)$, where Θ_D is the divergence network model parameter and I_{LR} is the LR image. I_D^i denotes i -th prediction of divergence network.

Deep Residual Structure. We construct relatively deeper residuals and apply residuals structure to all branches of our tree-based divergence network. In addition to the residuals within the residual group and the residuals from the input features to the end branches, we also add the residuals from intermediate branches to their own sub-branches as shown in Fig. 2. Residual learning address the problem of long-term memory in deep SR network. Therefore, inspired by previous works [10, 12, 33], we utilize deep residual structure to achieve more performance gain. We validate the effect of deep residual structure in Sec. 4.4.

Divergence loss. Divergence loss used in divergence network, which composed of L_2 loss and modified triplet loss. The L_2 loss can be defined as

$$L_2^D = \sum_{i=1}^P \left\| I_D^i - I_{HR} \right\|_2. \quad (1)$$

In order to make the divergence network produce divergence results, we use triplet loss between all pairs of different predictions from divergence network. Our goal is to make the distance between I_D^i and HR close and the distance between different members within I_D farther. However, using triplet loss directly on RGB images causes the network to focus more on other differentiated directions (e.g., RGB space and luminance) than texture features. Therefore, we perform a series of processes on the triplet inputs as shown in Fig. 2. Firstly, we process I_D^i using $G(\cdot)$:

$$G(I_D^i) = \frac{Y_D^i - \mu_{Y_D^i}}{\sigma_{Y_D^i}}, \quad (2)$$

where Y_D^i is Y channel of I_D^i in YCbCr space, $\mu_{Y_D^i}$ and $\sigma_{Y_D^i}$ are mean and standard deviation of Y_D^i respectively. $G(\cdot)$ operation can make the network enable to focus more on the differentiation of texture space rather than color and luminance space. Secondly, the triplet inputs are converted

to the residual domain where texture differences can be better represented. We express the residual of I_D^i as

$$res_{I_D^i} = \left| G(I_D^i) - G(I_{HR}) \right|, \quad (3)$$

where $|\cdot|$ is absolute value function. It can reduce the checkerboard phenomenon caused by triplet loss, which is discussed in Sec. 4.4. The formula for triplet loss is

$$trip(a, p, n) = \text{Max}[d(a, p) - d(a, n) + margin, 0], \quad (4)$$

where a , p and n are anchor, positive and negative, respectively. Therefore, we can represent our final triplet loss as

$$T_D = \frac{\sum_{i=1}^P \sum_{j=1, j \neq i}^P \beta_{ij} * trip(res_{I_D^i}, zero, res_{I_D^j})}{(P(P-1))}, \quad (5)$$

where $zero$ is zero map and it is the positive in residual domain. β is a attenuation coefficient which can be described as

$$\beta_{ij} = \theta^{l-1}, l \in [1, L], \quad (6)$$

where θ is parameter and $\theta \in (0, 1]$. The l is index of the tree depths where the common parent branch of I_D^i and I_D^j is located. We use β because that in a tree structure, differentiation should be progressive, i.e., branches with closer relatives should have relatively smaller degrees of divergence. Finally, our divergence loss is described as

$$L_D = L_2^D + \alpha * T_D, \quad (7)$$

where α is weight hyperparameter of T_D . Some detailed parameter settings will be introduced in Sec. 4.1.

3.3. Convergence Network

Combining the divergence results generated by the divergence network can produce more accurate results. We think that different areas on the predictions have different contribution weights for the final result. So we construct convergence network to merge divergent predictions weighted pixel-by-pixel, which can generate the result closer to the real HR image. Convergence network concatenates all the P predictions of the divergence network and outputs weight map for each prediction I_D^i . Weight maps can be expressed as $W = F(\text{Concat}(I_D); \Theta_C)$, where Θ_C is the convergence network model parameter. We denote W_i as the weight map of I_D^i . Every I_D^i are element-wise multiplied by respective weight map W_i , and then all of the results are summed to produce the final SR result. Accordingly, SR result can be defined as

$$I_{SR} = \sum_{i=1}^P (I_D^i \cdot W_i), \quad (8)$$

where I_{SR} represents final SR result.

Method	RealSR						DRealSR (train on RealSR)						D2CRealSR	
	x2		x3		x4		x2		x3		x4		x8	
	PSNR	SSIM	PSNR	SSIM	PSNR	SSIM	PSNR	SSIM	PSNR	SSIM	PSNR	SSIM	PSNR	SSIM
Bicubic	31.67	0.887	28.61	0.810	27.24	0.764	32.67	0.877	31.50	0.835	30.56	0.820	27.74	0.822
DRCN [11]	33.42	0.912	30.36	0.848	28.56	0.798	32.46	0.873	31.58	0.838	30.14	0.816	29.99	0.833
SRResNet [12]	33.17	0.918	30.65	0.862	28.99	0.825	32.85	0.890	31.25	0.841	29.98	0.822	30.01	0.864
EDSR [13]	33.88	0.920	30.86	0.867	29.09	0.827	32.86	0.891	31.20	0.843	30.21	0.817	30.23	0.868
RCAN [33]	33.83	0.923	30.90	0.864	29.21	0.824	32.93	0.889	31.76	0.847	30.37	0.825	30.26	0.868
ESRGAN [26]	33.80	0.922	30.72	0.866	29.15	0.826	32.70	0.889	31.25	0.842	30.18	0.821	30.06	0.865
SR-Flow [14]	-	-	-	-	24.20	0.71	-	-	-	-	24.97	0.73	23.11	0.600
LP-KPN [5]	33.49	0.917	30.60	0.865	29.05	0.834	32.77	-	31.79	-	30.75	-	-	-
CDC [28]	33.96	0.925	30.99	0.869	29.24	0.827	32.80	0.888	31.65	0.847	30.41	0.827	30.02	0.841
D2C-SR(Ours)	34.40	0.926	31.33	0.871	29.72	0.831	33.42	0.892	31.80	0.847	30.80	0.825	30.55	0.871

Table 1. Performance comparison on RealSR [5], DRealSR [28] and our proposed D2CRealSR datasets. Best and second best are marked in red and blue. ‘-’ indicates either the available model is not supported for such a test, or the method is not open-sourced.

Convergence loss. The goal of convergence network is to merge I_D^i from divergence network. Therefore, loss function of convergence network is called convergence loss, which only consists of L_2 loss. We denote convergence loss as L_2^C , which can be expressed as

$$L_2^C = \|I_{SR} - I_{HR}\|_2. \quad (9)$$

How to generate I_{SR} has been introduced in Eq. 8. The optimization goal of convergence loss is to make the generated SR image get close to the ground-truth HR image.

3.4. Training Strategy

The two networks in our framework are trained separately. We firstly train the divergence network into a stable status where it can generate super-resolution divergence predictions. We then freeze the parameters of divergence network and train the convergence network by enabling the whole pipeline. More details will be discussed in Sec. 4.1.

4. Experiment

4.1. Dataset and Implementation Details

D2CRealSR. The existing RealSR datasets generally include x2, x3 and x4 scaling factor only but lack of data for the larger scaling factor. We collect a new dataset on x8 scaling factor, which called D2CRealSR. We construct the LR and HR pairs by zooming the lens of DSLR cameras. D2CRealSR consists of 115 image pairs and 15 image pairs are selected randomly for testing set; the rest pairs construct the training set. We use SIFT method to register the image pairs iterative: we first register the image pairs roughly and crop the main central area, then we align the brightness of the central area of image pairs and register them once again. After that, we crop off the edges of aligned image pairs. The image size of each pair is $3,456 \times 2,304$ after the alignment process. We will release our D2CRealSR dataset later.

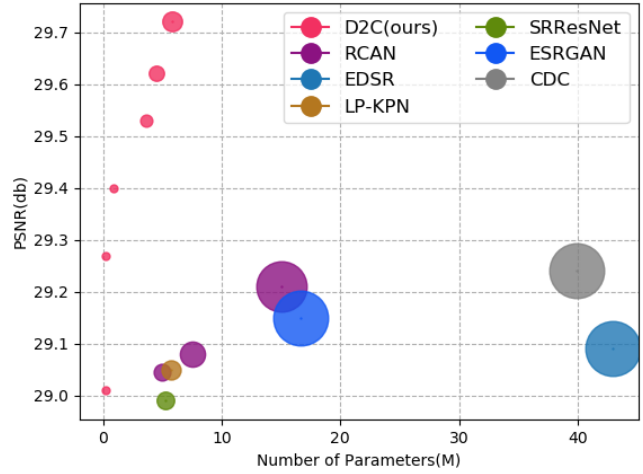


Figure 4. Comparison of performance vs. parameters. Our method uses fewer parameters to obtain better quantitative performance.

Existing datasets. We also conduct experiments on existing real-world SR datasets: RealSR and DRealSR. RealSR has 559 scenes captured from Nikon and Canon DSLR cameras and align the image pairs strictly. 459 scenes are selected for training and 100 scenes for testing. The image sizes of RealSR image pairs are in the range of 700~3000 and 600~3500. DRealSR has 83, 84 and 93 image pairs in testing set, 884, 783 and 840 image pairs in training set for x2, x3, x4 scaling factors, respectively. Note that we found some of the image pairs in DRealSR are misaligned, which is caused by the depth of field. So we only validate our results on testing set of DRealSR to show the performance of the cross-dataset of our method.

Implementation details. In the experiment, we set the number of branch layers as $L = 2$, the number of child branches $C = 2$. The basic branch module include $G = 2$ residual groups and $B = 4$ residual blocks in each group.

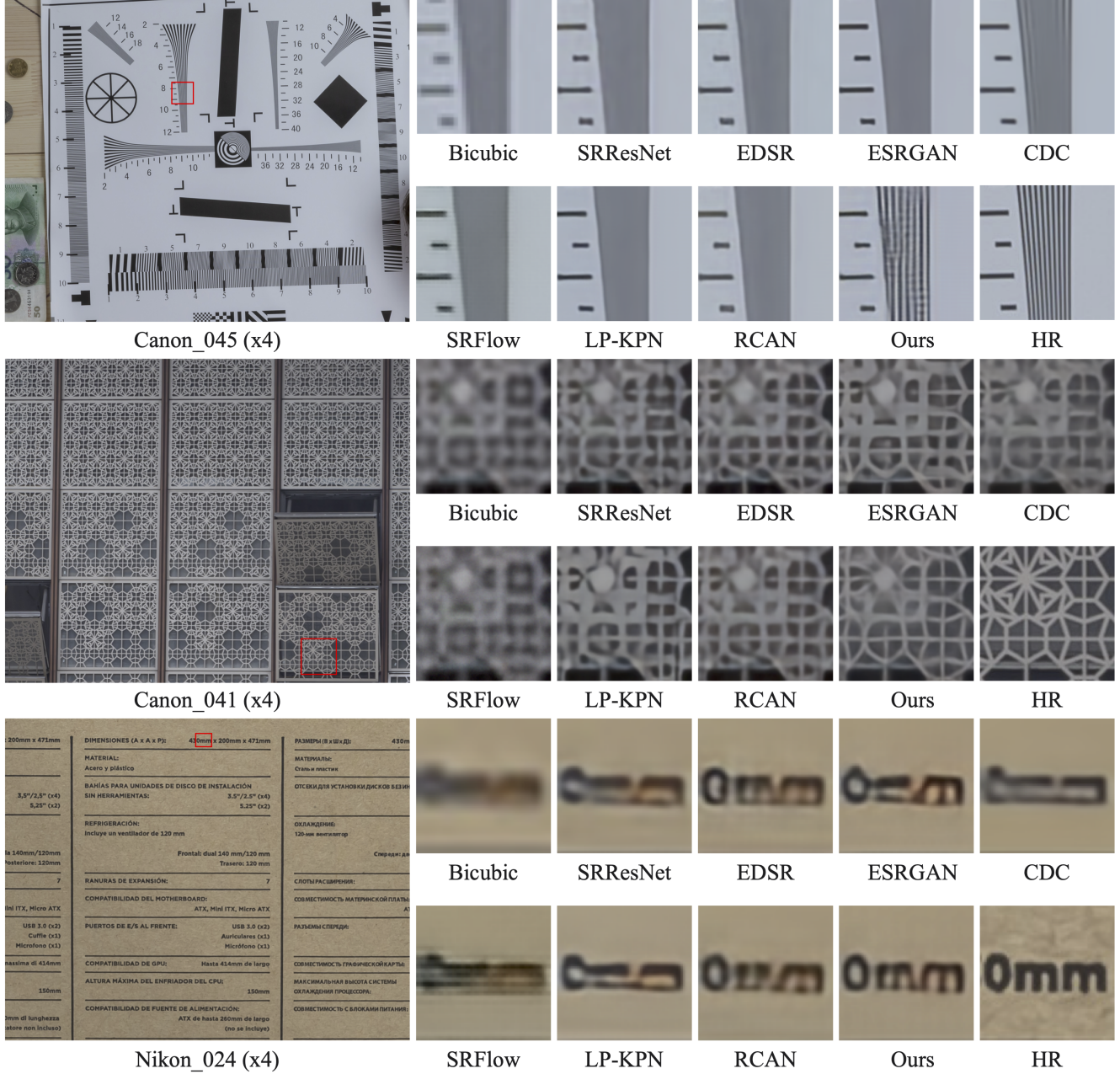


Figure 5. Visual comparison for x4 SR on RealSR [5] dataset. We compare Bicubic, SRResNet [12], EDSR [13], ESRGAN [26], SR-Flow [14], RCAN [33], LP-KPN [5], CDC [28] and our D2C-SR. Our results are consistently better than the compared methods. In particular, for the case Canon-045, only our method can recover the ‘stripe’ texture.

We use Adam optimizer and set exponential decay rates as 0.9 and 0.999. The initial learning rate is set to 10^{-4} and then reduced to half every $2k$ epochs. For each training batch, we randomly extract 4 LR image patches with the size of 96×96 . We implement D2C-SR method with the Pytorch framework and train the network using NVIDIA 2080Ti GPU.

4.2. Comparisons with Existing Methods

To evaluate our method, we train and test our model on our D2CRealSR with scaling factor x8 and an existing real-world SR dataset, RealSR with scaling factor x4, x3, x2. In addition, we validate on DRealSR testing set for performance of cross-dataset. We compare our model with other state-of-the-art SISR methods, including DRCN [11], SR-



Figure 6. Visual comparison for x8 SR on our captured D2CRealSR dataset. We compare SRResNet [12], EDSR [13], ESRGAN [26], SRFlow [14], RCAN [33], CDC [28] and our D2C-SR. Our method can produce sharper edges.

ResNet [12], EDSR [13], RCAN [33], ESRGAN [26], LP-KPN [5] and CDC [28]. The SISR results were evaluated on the Y channel in the YCbCr space using PSNR and SSIM. Among these SR methods, EDSR and RCAN are the classic SISR methods and DRCN is the open-source ensemble-based method. In addition, LP-KPN and CDC are designed to solve the real-world SR problem and they outperform on real-world SR benchmarks.

Quantitative comparison. The evaluation results of the SR methods, including our model and the other 8 methods are demonstrated in Table 1. Red numbers denote the highest scores, while blue numbers denote the second-highest scores. Our model outperforms by a large margin on all the benchmarks and achieve state-of-the-art performance.

Qualitative comparison. Visualization results of SR methods and ours on RealSR and D2CRealSR datasets are shown in Fig. 5 and Fig. 6. It is observed that existing SR methods (e.g., RCAN, LP-KPN, CDC) tend to restore the details to be thicker, blurry, or unnatural. Meanwhile, we restore more details than other methods. In Canon-045, only our method can recover the stripe texture. In Canon-041 and Sony-101, our method recovered sharper and more accurate edge textures. In Nikon-024, we recover more accurate information about the letters. From the visual comparison results, our method has the ability to recover richer and more accurate details.

4.3. Model Size Analyses

We show comparisons about model size and performance in Fig. 4. We list six sizes of models: 5.88M, 4.53M, 3.63M, 0.91M, 0.23M and 0.19M. These models are constructed by changing the number of residual groups G and

the number of residual block B . Our 0.23M model can achieve a better effect than other methods. At this PSNR level, CDC uses 39.92M, and RCAN also uses 15M parameters. Our baseline model achieve higher performance using 5.88M parameters only. Our method have a better trade-off between model size and performance.

	1	2	3	4
Width (C)	29.41	29.54	29.56	29.58
Depth (L)	29.30	29.54	29.63	29.64

Table 2. Effect study on the width and depth of the tree-based network (x4). As the depth or width increase, the performance of our method improves.

4.4. Ablation Studies

The width and depth of tree-based network. Our divergence network is a tree-based architecture. We set different L and C to provide experimental evaluations on the width and depth of the tree. Because increasing the depth and width increases memory usage. So we do these experiments on a small baseline model, which has $G = 2$ residual groups and each group has $B = 1$ block. As show in Table 2, we increase the width and depth from 1 to 4 respectively on x4 scaling factor and show the changes in PSNR. By increasing the width or depth of the tree-based network, the performance of our D2C-SR improves.

	x2		x3		x4	
	PSNR	SSIM	PSNR	SSIM	PSNR	SSIM
w/o. triplet loss	34.23	0.925	31.28	0.869	29.66	0.829
w/o. deep residual	34.28	0.925	31.28	0.870	29.68	0.830
D2C-SR(Ours)	34.40	0.926	31.34	0.871	29.72	0.831

Table 3. Effect of triplet loss and deep residual structure.

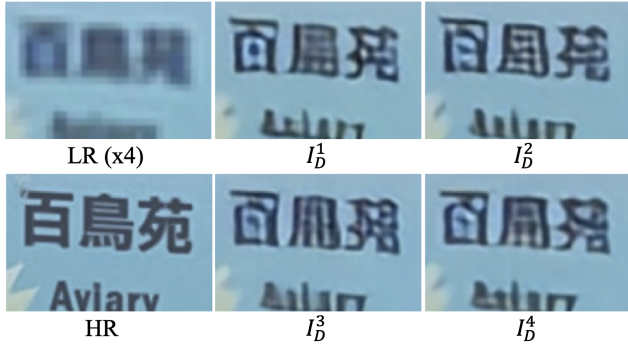


Figure 7. Visualization of the divergent predictions. The same row results has the same parent branch, so the results of different rows are relatively more divergent.

Triplet loss. As mentioned in Sec. 3.2, the triplet loss is used to enforce the outputs from different branches divergent. We further exam the effectiveness of our triplet loss by removing the term of Eq. 5. As show in Table 3 "w/o. triplet loss", PSNR scores in different scores are all decreased, especially in x2 scaling factor, the PSNR decreased 0.17 dB. Fig. 7 shows the visualization divergent results. As mentioned in the previous section, due to the existence of triplet loss, different end branches produce different texture predictions.

Deep residual structure. As mentioned in Sec. 3.2, we also disable the structure to verify its effectiveness. As show in Table 3 "w/o. deep res". It shows that the PSNR decreased without the deep residual structure.

Absolute value function and checkerboard. The input of absolute value function is the residual image, whose pixel value can oscillate between positive and negative. To remove such checkerboard effect, we involve absolute value function to smooth out different predictions generated by divergence loss as shown in Fig. 8.

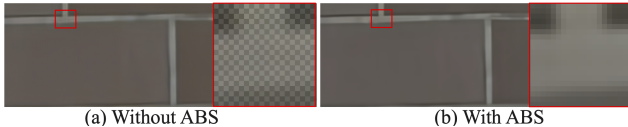


Figure 8. Absolute value function (ABS) in divergence loss can reduce the checkerboard phenomenon.

5. Conclusion

In this study, we revisit the problem of image super-resolution and provide a new two-stage approach: divergence stage for multiple predictions learning as well as convergence for predictions fusion. Instead of modeling the

entire distribution, we propose to learn a limited number of representative predictions and keep a sufficient divergence. This allows the network to be more efficient and achieves state-of-the-art performance with much less computational cost. We believe such divergence to convergence framework is a promising direction for image processing tasks like image inpainting as well as image denoising, and it is worth further exploration.

References

- [1] Saeed Anwar, Salman Khan, and Nick Barnes. A deep journey into super-resolution: A survey. *ACM Computing Surveys (CSUR)*, 53(3):1–34, 2020. [2](#)
- [2] Yuval Bahat and Tomer Michaeli. Explorable super resolution. In *Proc. CVPR*, pages 2716–2725, 2020. [3](#)
- [3] Marco Bevilacqua, Aline Roumy, Christine Guillenmot, and Marie Line Alberi-Morel. Low-complexity single-image super-resolution based on nonnegative neighbor embedding. In *Proc. BMVC*, 2012. [11](#)
- [4] Marcel C Buhler, Andrés Romero, and Radu Timofte. Deepsee: deep disentangled semantic explorative extreme super-resolution. In *Proc. ACCV*, 2020. [3](#)
- [5] Jianrui Cai, Hui Zeng, Hongwei Yong, Zisheng Cao, and Lei Zhang. Toward real-world single image super-resolution: A new benchmark and a new model. In *Proc. CVPR*, pages 3086–3095, 2019. [2](#), [3](#), [5](#), [6](#), [7](#), [10](#), [11](#), [12](#)
- [6] Chang Chen, Zhiwei Xiong, Xinmei Tian, Zheng-Jun Zha, and Feng Wu. Camera lens super-resolution. In *Proc. CVPR*, pages 1652–1660, 2019. [3](#), [10](#)
- [7] Dengxin Dai, Radu Timofte, and Luc Van Gool. Jointly optimized regressors for image super-resolution. In *Computer Graphics Forum*, volume 34, pages 95–104, 2015. [1](#), [2](#)
- [8] Ian J Goodfellow, Jean Pouget-Abadie, Mehdi Mirza, Bing Xu, David Warde-Farley, Sherjil Ozair, Aaron Courville, and Yoshua Bengio. Generative adversarial networks. *arXiv preprint arXiv:1406.2661*, 2014. [2](#)
- [9] Jinjin Gu, Hannan Lu, Wangmeng Zuo, and Chao Dong. Blind super-resolution with iterative kernel correction. In *Proc. CVPR*, pages 1604–1613, 2019. [3](#)
- [10] Jiwon Kim, Jung Kwon Lee, and Kyoung Mu Lee. Accurate image super-resolution using very deep convolutional networks. In *Proc. CVPR*, pages 1646–1654, 2016. [4](#), [11](#)
- [11] Jiwon Kim, Jung Kwon Lee, and Kyoung Mu Lee. Deeply-recursive convolutional network for image super-resolution. In *Proceedings of the IEEE conference on computer vision and pattern recognition*, pages 1637–1645, 2016. [2](#), [5](#), [6](#)

[12] Christian Ledig, Lucas Theis, Ferenc Huszár, Jose Caballero, Andrew Cunningham, Alejandro Acosta, Andrew Aitken, Alykhan Tejani, Johannes Totz, Zehan Wang, et al. Photo-realistic single image super-resolution using a generative adversarial network. In *Proc. CVPR*, pages 4681–4690, 2017. [2](#), [4](#), [5](#), [6](#), [7](#), [11](#), [12](#)

[13] Bee Lim, Sanghyun Son, Heewon Kim, Seungjun Nah, and Kyoung Mu Lee. Enhanced deep residual networks for single image super-resolution. In *Proc. CVPRW*, pages 136–144, 2017. [1](#), [2](#), [5](#), [6](#), [7](#), [11](#), [12](#)

[14] Andreas Lugmayr, Martin Danelljan, Luc Van Gool, and Radu Timofte. Srfow: Learning the super-resolution space with normalizing flow. In *Proc. ECCV*, pages 715–732, 2020. [2](#), [3](#), [5](#), [6](#), [7](#), [12](#)

[15] David Martin, Charless Fowlkes, Doron Tal, and Jitendra Malik. A database of human segmented natural images and its application to evaluating segmentation algorithms and measuring ecological statistics. In *Proc. ICCV*, volume 2, pages 416–423, 2001. [11](#)

[16] Pablo Navarrete Michelini, Hanwen Liu, and Dan Zhu. Multigrid backprojection super-resolution and deep filter visualization. In *Proceedings of the AAAI Conference on Artificial Intelligence*, volume 33, pages 4642–4650, 2019. [1](#)

[17] Zhihong Pan, Baopu Li, Teng Xi, Yanwen Fan, Gang Zhang, Jingtuo Liu, Junyu Han, and Errui Ding. Real image super resolution via heterogeneous model ensemble using gp-nas. In *European Conference on Computer Vision*, pages 423–436. Springer, 2020. [2](#)

[18] Mehdi SM Sajjadi, Bernhard Scholkopf, and Michael Hirsch. Enhancenet: Single image super-resolution through automated texture synthesis. In *Proc. ICCV*, pages 4491–4500, 2017. [2](#)

[19] Wenzhe Shi, Jose Caballero, Ferenc Huszár, Johannes Totz, Andrew P Aitken, Rob Bishop, Daniel Rueckert, and Zehan Wang. Real-time single image and video super-resolution using an efficient sub-pixel convolutional neural network. In *Proc. CVPR*, pages 1874–1883, 2016. [2](#)

[20] Karen Simonyan and Andrew Zisserman. Very deep convolutional networks for large-scale image recognition. *arXiv preprint arXiv:1409.1556*, 2014. [1](#), [2](#)

[21] Dehua Song, Chang Xu, Xu Jia, Yiyi Chen, Chun-jing Xu, and Yunhe Wang. Efficient residual dense block search for image super-resolution. In *Proceedings of the AAAI Conference on Artificial Intelligence*, volume 34, pages 12007–12014, 2020. [1](#)

[22] Libin Sun and James Hays. Super-resolution from internet-scale scene matching. pages 1–12, 2012. [2](#)

[23] Radu Timofte, Vincent De Smet, and Luc Van Gool. Anchored neighborhood regression for fast example-based super-resolution. In *Proc. ICCV*, pages 1920–1927, 2013. [2](#)

[24] Radu Timofte, Vincent De Smet, and Luc Van Gool. A+: Adjusted anchored neighborhood regression for fast super-resolution. In *Proc. ACCV*, pages 111–126, 2014. [1](#), [2](#)

[25] Lingfeng Wang, Zehao Huang, Yongchao Gong, and Chunhong Pan. Ensemble based deep networks for image super-resolution. *Pattern recognition*, 68:191–198, 2017. [2](#)

[26] Xintao Wang, Ke Yu, Shixiang Wu, Jinjin Gu, Yihao Liu, Chao Dong, Yu Qiao, and Chen Change Loy. Esr-gan: Enhanced super-resolution generative adversarial networks. In *Proc. ECCVW*, pages 0–0. [2](#), [5](#), [6](#), [7](#), [12](#)

[27] Zhihao Wang, Jian Chen, and Steven CH Hoi. Deep learning for image super-resolution: A survey. 2020. [2](#)

[28] Pengxu Wei, Ziwei Xie, Hannan Lu, Zongyuan Zhan, Qixiang Ye, Wangmeng Zuo, and Liang Lin. Component divide-and-conquer for real-world image super-resolution. In *Proc. ECCV*, pages 101–117, 2020. [2](#), [3](#), [5](#), [6](#), [7](#), [10](#), [11](#), [12](#)

[29] Dongping Xiong, Qiuling Gui, Wenguang Hou, and Mingyue Ding. Gradient boosting for single image super-resolution. *Information Sciences*, 454:328–343, 2018. [2](#)

[30] Chih-Yuan Yang and Ming-Hsuan Yang. Fast direct super-resolution by simple functions. In *Proc. ICCV*, pages 561–568, 2013. [1](#), [2](#)

[31] Jianchao Yang, John Wright, Thomas Huang, and Yi Ma. Image super-resolution as sparse representation of raw image patches. In *Proc. CVPR*, pages 1–8, 2008. [1](#), [2](#)

[32] Xuaner Zhang, Qifeng Chen, Ren Ng, and Vladlen Koltun. Zoom to learn, learn to zoom. In *Proc. CVPR*, pages 3762–3770, 2019. [3](#), [10](#)

[33] Yulun Zhang, Kunpeng Li, Kai Li, Lichen Wang, Bineng Zhong, and Yun Fu. Image super-resolution using very deep residual channel attention networks. In *Proc. ECCV*, pages 286–301, 2018. [1](#), [4](#), [5](#), [6](#), [7](#), [11](#), [12](#)

A. Overview

In this supplementary material, we first introduce more details of our D2CRealSR dataset in Sec. B, including the collection method and the processing method. Then, we discuss simulated degradation and real-world degradation in Sec. C. In addition, we show the performance of our method on the bicubic datasets. In Sec. D, we demonstrate more experimental results, including the effect of triplet loss, the effect of deep residual structure, residual domain in the divergence loss and the weight maps at convergence stage. We all show the visualization results for these extra experiments in this sections. Finally, we show more visual comparison results and divergence results in Sec. E.

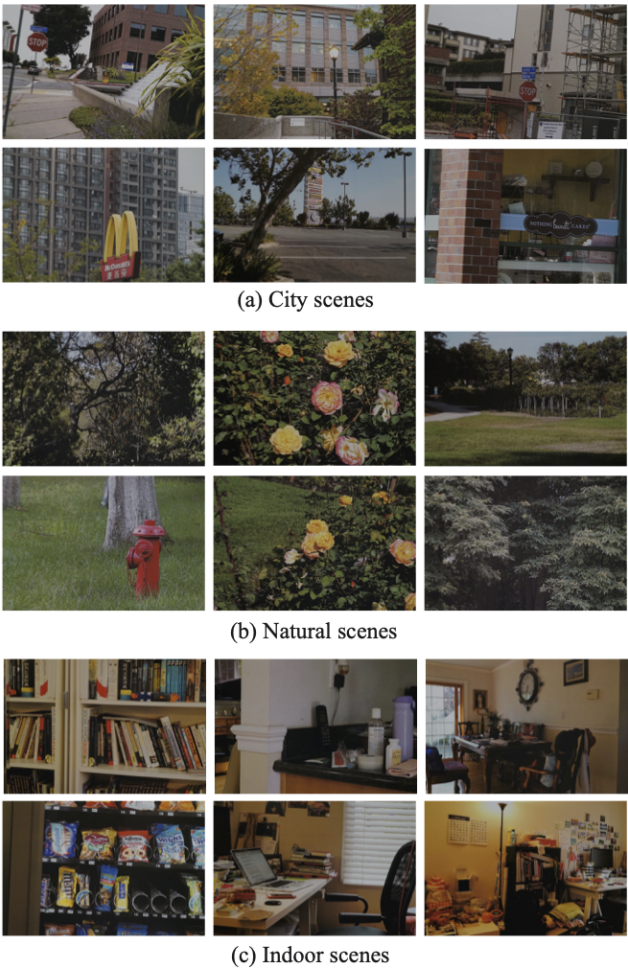


Figure 9. Examples of D2CRealSR dataset.

B. D2CRealSR Dataset

Existing real-world SISR datasets generally include images pairs on x2, x3 and x4 scaling factors, such as RealSR dataset [5] and DRealSR dataset [28]. Our proposed

D2CRealSR dataset have images pairs on x8 scaling factor, which larger than the existing real-world datasets. The ill-posed problem is more obvious on D2CRealSR dataset.

Images pairs in our dataset are taken by zooming Sony α -7. The number of training pairs in our dataset is 100, and testing set has 15 images pairs selected randomly. The D2CRealSR provides, to the best of our knowledge, the first general purpose benchmark on x8 scaling factor for real-world SISR. It is difficult to obtain images pairs with good alignment effects in natural scenes. These difficulties in the alignment process include depth-of-field misalignment, noticeable perspective misalignment, lens distortion misalignment and resolution alignment ambiguity [32]. Therefore, using the DSLR camera to directly acquire natural scene images pairs generally cannot be well aligned. We have found misalignment in DRealSR dataset, mostly due to depth-of-field misalignment. To solve these misalignment problems, we collect some high-resolution images, firstly. These images are mostly taken by DSLR from existing datasets or our own shooting dataset. Different from City100 [6], which only have city scenes, we have selected the images with different scenes including indoor and outdoor. It contains a variety of target objects with rich texture. Then, we print these scenes on high-quality postcards just like City100, and we get images pairs by taking photos of postcards. For each scaling factors, we measured a safety distance under a controlled environment in professional laboratory such that the textures and reflections of postcards have no effect on the captured data. These postcards are on a fixed plane, which can reduce the influence of depth-of-field misalignment. It also weakens noticeable perspective misalignment. Further, we blur the HR images of pairs in during calculating matrix M in SIFT algorithm and apply the M on the source HR images to align source HR images with LR images. In this way, it can weaken the influence of resolution alignment ambiguity. We use multiple iterative alignment methods to ensure alignment results. Cropping the center area after each alignment can reduce misalignment caused by lens distortion. Several examples of our D2CRealSR dataset are shown in Fig. 9, and it will be made publicly available later.

C. Simulated SISR and Real-World SISR

As shown in Fig. 10, real-world degradation loses more information than bicubic compared with the HR, which also have been discussed in [6]. The bicubic downsampling datasets contains more prior information than real-world datasets on the same scaling factor and ill-posed problem becomes more apparent. Therefore, the real-world datasets can better reflect the effectiveness of our method and our approach allows for more performance gains on real-world datasets. Nevertheless, as shown in Table 4, we still achieve good performance on bicubic benchmarks. Recently, more

works have focused on real-world SR because the great gap between simulated and real-world degradation hinders practical SR applications[5, 28]. Therefore, our approach focuses primarily on real-world SR.

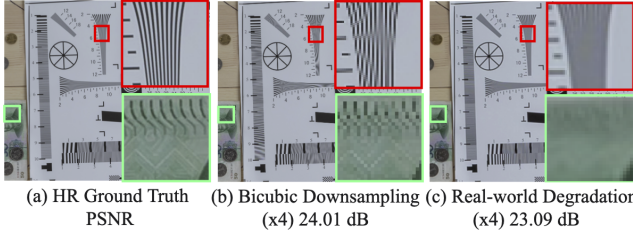


Figure 10. Comparison of bicubic degradation and real-world degradation at the same scaling factor (x4). Real-world degradation loses more information than bicubic degradation.

Method	x2		x3		x4		x8		
	PSNR	SSIM	PSNR	SSIM	PSNR	SSIM	PSNR	SSIM	
Set5	Bicubic	33.66	0.9299	30.39	0.8682	28.42	0.8104	24.40	0.6580
	SRCNN	36.66	0.9542	32.75	0.9090	30.48	0.8628	25.33	0.6900
	FSRCNN	37.05	0.9560	33.18	0.9140	30.72	0.8660	20.13	0.5520
	VDSR	37.53	0.9590	33.67	0.9210	31.35	0.8830	25.93	0.7240
	LapSRN	37.52	0.9591	33.82	0.9227	31.54	0.8850	26.15	0.7380
	MemNet	37.78	0.9597	34.09	0.9248	31.74	0.8893	26.16	0.7414
	EDSR	38.11	0.9602	34.65	0.9280	32.46	0.8968	26.96	0.7762
	SRMDNF	37.79	0.9601	34.12	0.9254	31.96	0.8925	-	-
	D-DBPN	38.09	0.9600	-	-	32.47	0.8980	27.21	0.7840
	RDN	38.24	0.9614	34.71	0.9296	32.47	0.8990	-	-
B100	RCAN	38.27	0.9614	34.74	0.9299	32.63	0.9002	27.31	0.7878
	Ours	38.26	0.9619	34.72	0.9302	32.62	0.8999	27.46	0.7814
	Bicubic	29.56	0.8431	27.21	0.7385	25.96	0.6675	23.67	0.5480
	SRCNN	31.36	0.8879	28.41	0.7863	26.90	0.7101	24.13	0.5660
	FSRCNN	31.53	0.8920	28.53	0.7910	26.98	0.7150	24.21	0.5680
B100	VDSR	31.90	0.8960	28.83	0.7990	27.29	0.7260	24.49	0.5830
	LapSRN	31.08	0.8950	28.82	0.7980	27.32	0.7270	24.54	0.5860
	MemNet	32.08	0.8978	28.96	0.8001	27.40	0.7281	24.58	0.5842
	EDSR	32.32	0.9013	29.25	0.8093	27.71	0.7420	24.81	0.5985
	SRMDNF	32.05	0.8985	28.97	0.8025	27.49	0.7337	-	-
	D-DBPN	32.27	0.9000	-	-	27.72	0.7400	24.88	0.6010
	RDN	32.34	0.9017	29.26	0.8093	27.72	0.7419	-	-
	RCAN	32.41	0.9027	29.32	0.8111	27.77	0.7436	24.98	0.6058
	Ours	32.41	0.9041	29.28	0.8125	27.77	0.7466	24.98	0.6140

Table 4. Quantitative comparison on bicubic downsampling datasets (Set5 [3] and B100 [15]).

D. More Experimental Results

D.1. Effect of Triplet Loss

Our approach explicitly models the distribution of high-frequency details using a discrete manner, and the triplet loss is the key to achieve our modeling ways. In Fig. 13, we show the comparison of visual results using different weighting coefficient α of triplet loss. In these results, we can intuitively see that as the coefficients α increase, the divergences effect between different branches becomes more and more pronounced, and also produces accurate texture details. In contrast, without the use of triplet loss, the branches produce similar and blurred results.

D.2. Effect of Deep Residual Structure

In Fig. 14, we show the effect of deep residuals on the results. Like some works descriptions [10, 33], residual learning address the problem of long-term memory in deep SR network, so we can get sharper results as demonstrated in the experiment.

D.3. Residual Domain in Divergence Loss

In Fig. 11, we show the visualization of the results after computing the residuals between HR and SR prediction in divergence loss. Residual results have a higher response in the high-frequency region. Therefore, adding residual processing to the divergence loss allows the divergence predictions to focus more on high-frequency texture regions, which is exactly what we want to achieve.

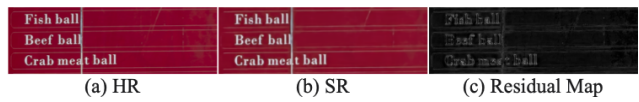


Figure 11. The visualization result of residuals in divergence loss on x4 scaling factor.

D.4. Visualization of Weight Maps

As mentioned before, we assign spatial weights to the divergence results and use this weight for the fusion of the divergence results at the convergence stage. In Fig. 15, we visualize the weight maps using the heatmap. The visualization results show that predictions have their own weights in different spatial locations during the merge process.

E. More Visual Results

E.1. More Visual Comparison Results on RealSR Dataset

We show more visual comparison results in Fig. 12. Our method is compared with other methods, SRResNet [12], EDSR [13], RCAN [33], CDC [28] and LP-KPN [5]. As shown in the figure, our proposed D2C-SR framework can restore more reasonable prediction results. Other classic super-resolution methods produce unnatural results due to the ill-posed problem.

E.2. More Visual Results on D2CRealSR Dataset

In Fig. 16, we show more visual results from our proposed D2C-SR method on D2CRealSR dataset. We crop the images pairs and show the patch to facilitate the presentation of image details. The LR images patches are upsampled using bicubic method.

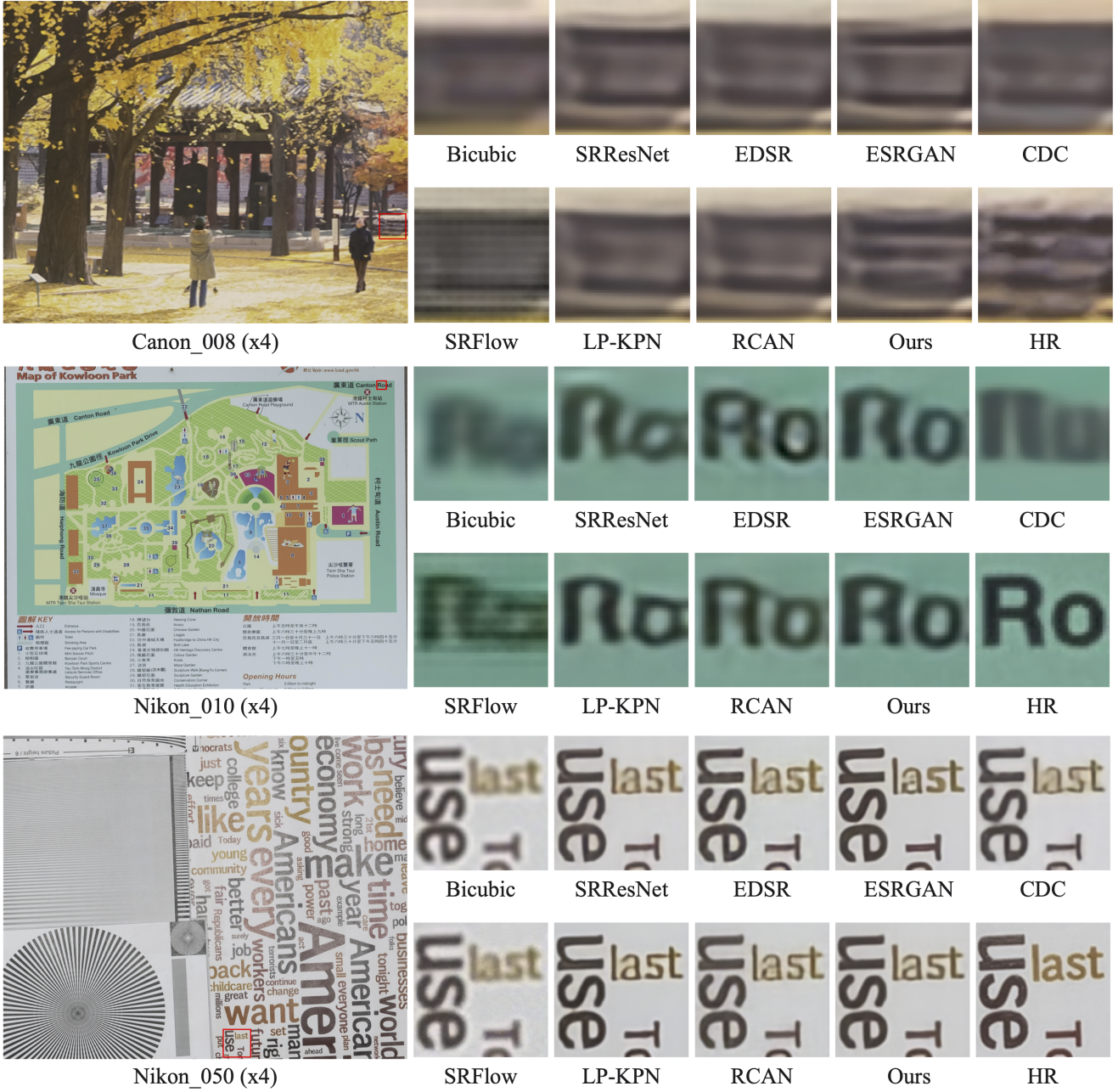


Figure 12. More Visual comparison for x4 SR on RealSR [5] dataset. We compare Bicubic, SRResNet [12], EDSR [13], ESRGAN [26], SRFlow [14], RCAN [33], LP-KPN [5], CDC [28] and our D2C-SR.

E.3. More Visual Divergence Results

We show more visual divergence results in Fig. 17. We also crop the images pairs, and the LR images patches are up-sampled using bicubic method. In the high-frequency detail region our method significantly produces a divergence of results.

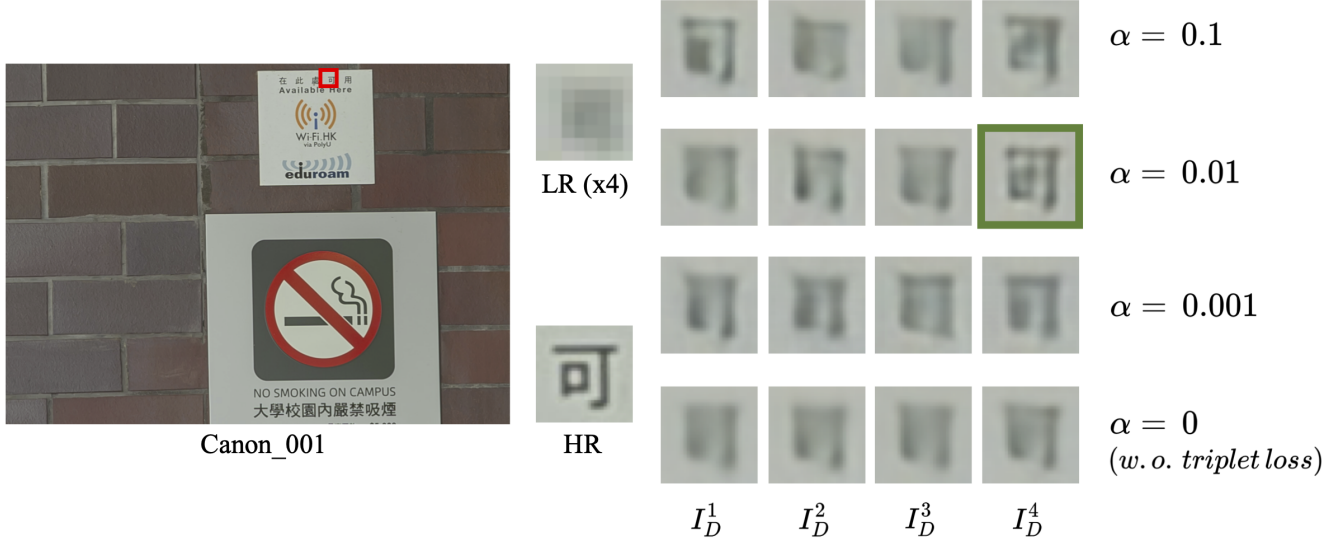


Figure 13. Comparison of visual results using different weighting coefficient α of triplet loss. It can be seen that the results are relatively similar and blurred when triplet loss is not used. As the coefficients α increase, the divergent effect of each branch becomes more and more obvious, and the results containing richer and more accurate high-frequency details appear.

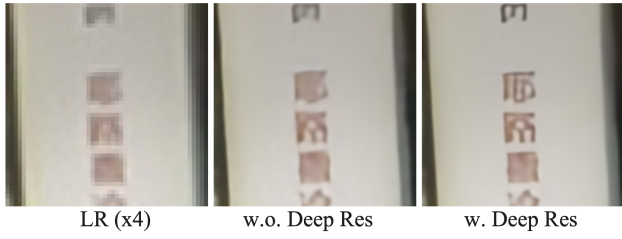


Figure 14. Demonstrate the visual comparison results of deep residual structure impact.

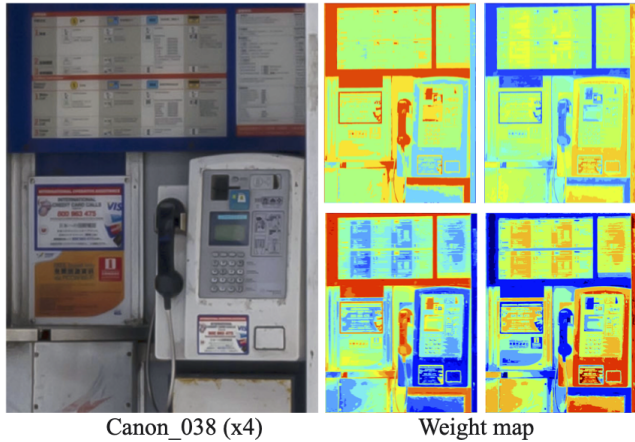


Figure 15. Weight maps in our convergence stage. Red indicates higher values, while the blue indicates lower values. Each row belongs to the same parent branch predictions. (Our basemodel $L = 2, C = 2$).

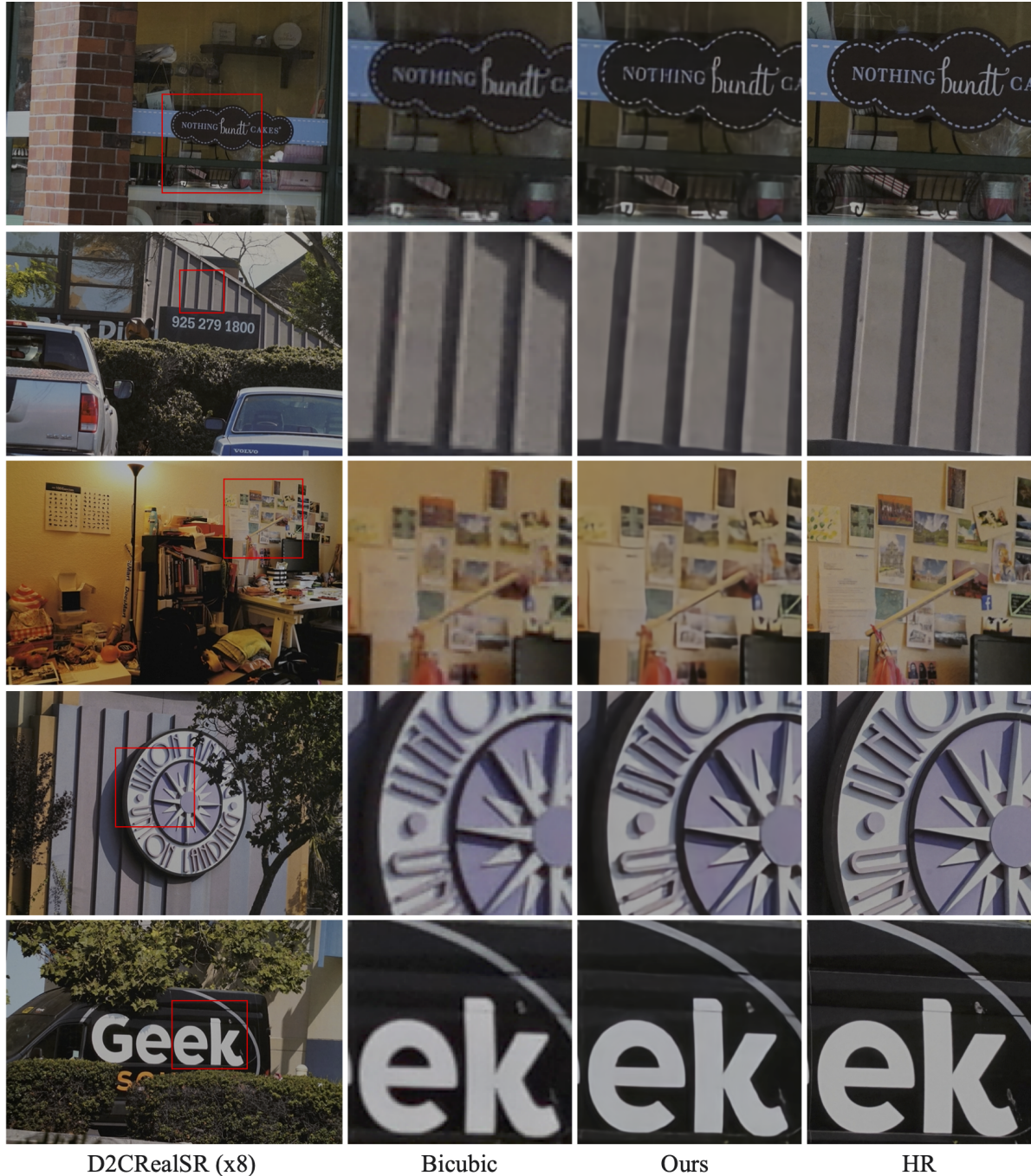


Figure 16. More visual results on D2CRealSR dataset.

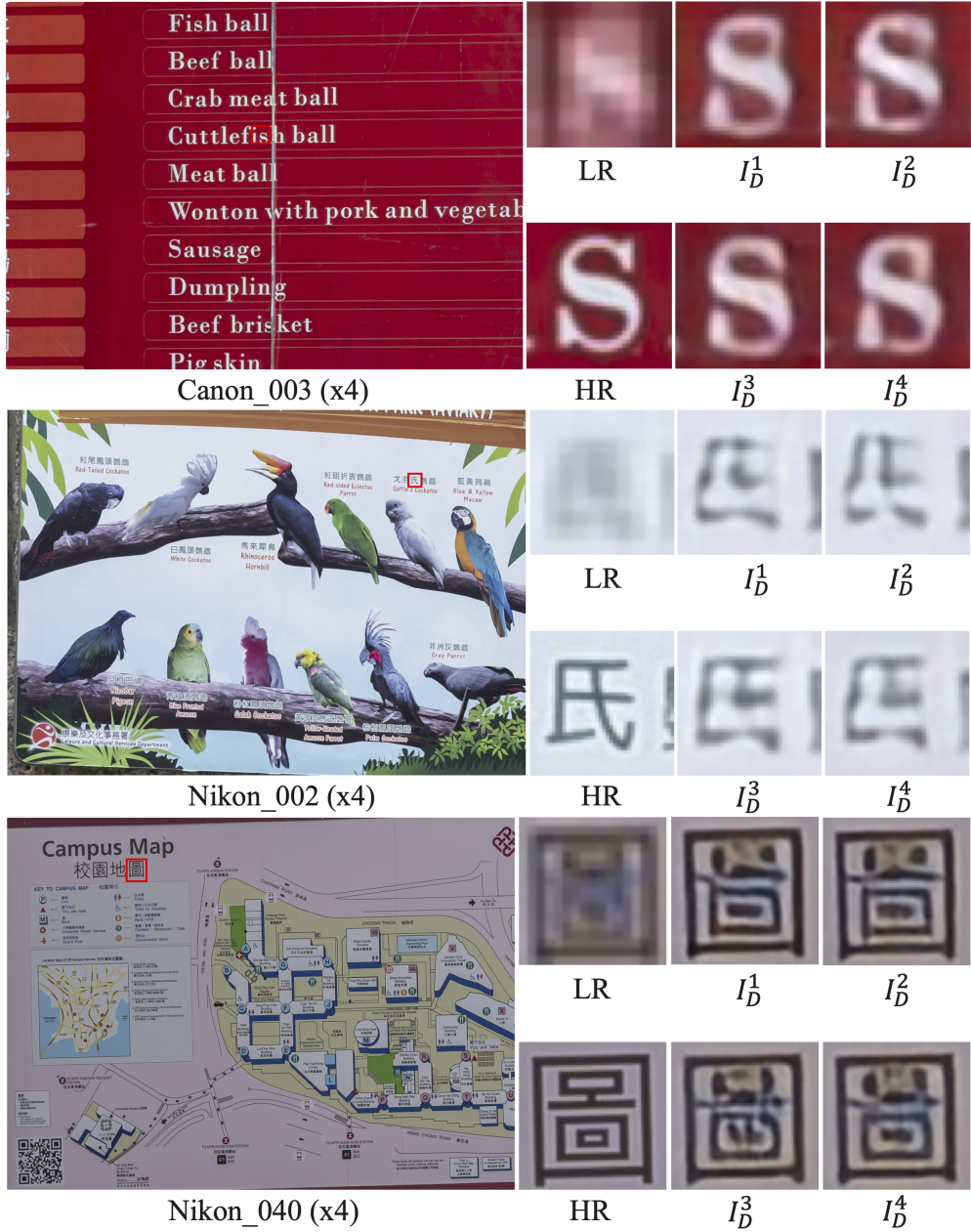


Figure 17. More visual divergence results. Our method produces differentiated results in the high-frequency texture region, due to the presence of triplet loss.